PERGAMON

Available online at www.sciencedirect.com

SCIENCE DIRECT®

International Journal of Impact Engineering 28 (2003) 391–411

INTERNATIONAL JOURNAL OF IMPACT ENGINEERING

www.elsevier.com/locate/ijimpeng

A unified model for long-rod penetration in multiple metallic plates

S. Chocron[a], C.E. Anderson Jr.[b,*], J.D. Walker[b], M. Ravid[c]

[a] *Dpto. Ciencia de Materiales, E.T.S.I. Caminos, Univ. Politécnica de Madrid, Madrid 28040, Spain*
[b] *Engineering Dynamics Department, Southwest Research Institute, P.O. Box 28510, San Antonio, TX 78228-0510, USA*
[c] *Rimat Advanced Technologies, 8B Simtat Hayerek, Hod Hasharon, Israel*

Received 8 November 2001; accepted 23 July 2002

Abstract

The Walker–Anderson and Ravid–Bodner analytical models for penetration of projectiles in metallic plates are well known in the ballistics community. The Walker–Anderson model uses the centerline momentum balance in the projectile and target to calculate the penetration history into a semi-infinite medium, while the Ravid–Bodner model uses the upper bound theorem of plasticity theory modified to include dynamic effects. The Ravid–Bodner model also includes a rich selection of failure modes suitable for finite-thick metallic targets. In this paper a blended model is presented: momentum balance is used to calculate the semi-infinite portion penetration (before the back of the target plate begins to flow), and the Ravid–Bodner failure modes are used to determine projectile perforation. In addition, the model has been extended to handle multiple plate impact. Numerical simulations show that after target failure the projectile still continues to erode for some microseconds. This time has been estimated and incorporated into the model. Examples are presented for long-rod projectiles against thick and spaced-plate targets backed by a witness pack that is separated from the main target element(s) by an air gap. Agreement with results from numerical simulations is quite good.

© 2002 Elsevier Science Ltd. All rights reserved.

Keywords: Penetration mechanics; Analytical modeling; Multiple-plate impact; Walker–Anderson model; Ravid–Bodner model; Failure modes

1. Introduction

The Walker–Anderson analytical penetration model [1] predicts the penetration of long rods into semi-infinite metallic targets by using the centerline momentum balance with certain plasticity

---

*Corresponding author. Tel.: +1-210-522-2313; fax: +1-210-522-6290.
E-mail address: canderson@swri.edu (C.E. Anderson Jr.).

0734-743X/02/$ - see front matter © 2002 Elsevier Science Ltd. All rights reserved.

PII: S0734-743X(02)00069-6

Nomenclature

c'	velocity of the elastic–plastic interface
c	speed of sound in projectile
c_0	bulk sound speed (target)
c_p	auxiliary variable
D	projectile diameter
G_t	shear modulus (target)
H_b	bulge height (see Fig. 2)
k	slope of Hugoniot relation
K_0	ambient bulk modulus
$K_\mathrm{t}(t)$	bulk modulus (target)
$L(t)$	projectile length
R	crater (penetration channel) radius
R_p	projectile radius
$s(t)$	plastic extent in projectile
T	target thickness
$u(t)$	penetration velocity
U_2	auxiliary variable
u_z	centerline velocity
$v(t)$	tail velocity of projectile
V_0	impact velocity
Y_t	target flow stress
z_i	position of projectile–target interface
$Z_\mathrm{i}, Z_\mathrm{pen}, Z_\mathrm{T}$	bulge advancement
z_p	Position of projectile tail

Greek symbols

$\alpha(t)$	Extent of the plastic zone in the target
η_b	radial extent of bulge
ε_cr	critical strain
η_0	max extent of bulge
ε^p	equivalent plastic strain
σ_{xz}	shear stress in target
β	angle (see Fig. 2)
ρ_p	projectile density
ρ_t	target density
σ_p	projectile flow stress
χ	auxiliary variable
ζ	auxiliary variable

assumptions. Key assumptions are that the velocity profiles in the projectile and target are specified, and that the shear stress within the target can be evaluated from a hemispherical flow field, which is calculated from the curl of a vector potential (thus insuring the incompressibility of plastic flow). It can be shown in the limit as the three-dimensional terms are allowed to go to zero, and the transient terms ignored (i.e. steady-state conditions) that the one-dimensional model of Tate and Alekseevskii is recovered, although the Walker–Anderson model predicts a priori the penetration resistance of the target, whereas the term is empirical in the original work of Tate and Alekseevskii.

Ravid and Bodner [2], in their penetration model, postulate flow fields for different regions of the target. A variational procedure is used to determine the longitudinal and radial extent of plastic deformation (combined with compatibility conditions between the various flow zones). The Ravid–Bodner model deals with finite-thickness metallic targets by considering seven different exit modes that can take into account a range of failure modes, such as petalling, plugging, etc. (The initial work by Ravid and Bodner [2] considered the projectile to be rigid, but they later extended their model to an eroding projectile [3]. However, the exit modes represent a response of the target material, and are therefore independent of whether the projectile is rigid or eroding.)

This paper presents a blend between the Walker–Anderson and Ravid–Bodner models. This "unified" model uses the momentum balance equation to calculate at each time step the penetration velocity of the projectile. The different exit modes proposed by Ravid et al. [4] were added assuming that the target could fail only when the plastic extent reaches the rear target surface.

There was also an objective to make the model applicable to multiple-plate penetration problems. Numerical simulations were performed to study multiple-plate interactions. The simulations clearly show that erosion and deformation of the projectile continues some microseconds after target failure due to stress gradients that exist in the projectile nose area after perforation. In this work, it is assumed that stress relaxation (meaning the elimination of stress gradients due to rarefaction waves from the stress-free surface, and velocity equilibration of the projectile) occurs at the rate observed in the numerical simulations. To check the model, examples are presented for long-rod projectiles against thick targets, thick targets backed by a witness pack, as well as a spaced-plate target backed by a witness pack. Agreement with experimental results and numerical simulations is considered to be quite good.

2. Analytical model

2.1. First phase: penetration into semi-infinite target

The Walker–Anderson model [1] is based on a centerline momentum balance. Target resistance is based on a three-dimensional flow field[1] combined with rigid-plastic assumptions for the constitutive response of the plastically flowing target material. Effects of target compressibility are included in the extent of the flow field. Since the centerline momentum equation is central to the model, it is given here, and other equations are included within the individual subsections as necessary. The integral of the time-dependent momentum equation, along the projectile–target centerline, is evaluated to calculate the penetration history. The problem is assumed axially symmetric, with the z-coordinate denoting the direction of penetration

---

[1] The flow field is three-dimensional, and an (r, θ, z) coordinate system is used to describe the flow field [1]. However, axial symmetry considerations permit some simplification, so it might be argued that the flow field is "two-dimensional."

$$\rho_{\mathrm{p}} \int_{z_{\mathrm{p}}}^{z_{\mathrm{i}}} \frac{\partial u_z}{\partial t}\,\mathrm{d}z + \rho_{\mathrm{t}} \int_{z_{\mathrm{i}}}^{+\infty} \frac{\partial u_z}{\partial t}\,\mathrm{d}z + \frac{1}{2}\rho_{\mathrm{p}} u_z^2\Big|_{z_{\mathrm{p}}}^{z_{\mathrm{i}}} + \frac{1}{2}\rho_{\mathrm{t}} u_z^2\Big|_{z_{\mathrm{i}}}^{+\infty} - \sigma_{zz}|_{z_{\mathrm{p}}}^{+\infty} - 2\int_{z_{\mathrm{p}}}^{+\infty} \frac{\partial \sigma_{xz}}{\partial x}\,\mathrm{d}z = 0 \tag{1}$$

In Eq. (1), the integration interval z_{p} to z_{i} evaluates the momentum equation from the tail of the projectile (z_{p}) to the projectile–target interface (z_{i}). The integration interval z_{i} to $+\infty$ evaluates the momentum equation from the projectile–target interface into the target, which is assumed to be semi-infinite.

The basic equations and assumptions for evaluating the various terms of Eq. (1), as well as the explicit expressions for the flow fields are described in Walker and Anderson [1]. Performing the integrations—using a bilinear velocity profile in the projectile, hemispherical flow in the target, and the Von Misses flow rule—leads to the following equation:

$$\begin{aligned} &\rho_{\mathrm{p}}\dot{v}(L-s) + \dot{u}\left\{\rho_{\mathrm{p}} s + \rho_{\mathrm{t}} R\frac{\alpha-1}{\alpha+1}\right\} + \rho_{\mathrm{p}}\frac{\mathrm{d}}{\mathrm{d}t}\left(\frac{v-u}{s}\right)\frac{s^2}{2} + \rho_{\mathrm{t}}\dot{\alpha}\frac{2Ru}{(\alpha+1)^2} \\ &\quad = \tfrac{1}{2}\rho_p(v-u)^2 - \left\{\tfrac{1}{2}\rho_{\mathrm{t}}u^2 + \tfrac{7}{3}Y_{\mathrm{t}}\ln\alpha\right\}, \end{aligned} \tag{2}$$

where the dot over a symbol denotes the time derivative of the variable. Elastic waves between the tail and the elastic–plastic interface in the projectile result in deceleration of the projectile tail

$$\dot{v} = -\frac{\sigma_{\mathrm{p}}}{\rho_{\mathrm{p}}(L-s)}\left\{1 + \frac{v-u}{c} + \frac{\dot{s}}{c}\right\}. \tag{3}$$

The erosion rate of the projectile is given by the geometric condition

$$\dot{L} = -(v-u). \tag{4}$$

The plastic extent, s, in the projectile is calculated assuming that the velocity profile and its derivative are continuous at the projectile–target interface

$$s = \frac{R}{2}\left(\frac{v}{u} - 1\right)\left(1 - \frac{1}{\alpha^2}\right). \tag{5}$$

The radius of the penetration crater is calculated from an equation fit to experimental data

$$R = R_{\mathrm{p}}(1 + 0.287V_0 + 0.148V_0^2). \tag{6}$$

The bulk modulus is assumed to vary with penetration velocity according to

$$K_{\mathrm{t}} = K_0\left(1 + k\frac{u}{c_0}\right)^2. \tag{7}$$

At this point, given the initial impact velocity, this system of equations can be solved to determine the penetration-time history provided the extent of plastic flow, given by αR, can be determined. Compressible cylindrical cavity expansion provides an estimate for α;[2] [1] α is solved as a function of the penetration velocity from the transcendental equation

---

[2] It was demonstrated by Chocron et al. [5], that cylindrical cavity expansion provides a more accurate estimate of the extent of plastic flow than spherical cavity expansion.

$$\left(1+\frac{\rho_t u^2}{Y_t}\right)\sqrt{K_t-\rho_t u^2\alpha}=\left(1+\frac{\rho_t u^2\alpha^2}{2G_t}\right)\sqrt{K_t-\rho_t u^2}. \tag{8}$$

Eqs. (2)–(8) are solved simultaneously to give the penetration history as a function of time. Input parameters are the impact velocity and the respective material properties for the projectile and target.

2.2. Second phase: bulging and perforation

The Walker–Anderson model, described by the series of equations above, is operative up to the penetration depth where the rear surface affects the penetration process. From this point on, modifications are required to account for and model the perforation mechanics. When the exit descriptions of Ravid and Bodner [2] are adapted to the penetration model, bulge formation and advancement are defined and possible failure modes can be analyzed. Various failure mechanisms can cause target failure and perforation including ejected target mass in the form of a conical plug (when shear effects are dominant) or a spherical cap (when ductile effects dominate). The possibility of ejection of a frontal conical sector in the form of a defined fragment cloud (debris) including the mass and spatial distribution of a fragmentation cone can also be analyzed.

2.2.1. Transition to exit stages

The semi-infinite penetration model is assumed to be operative up to the point Z_T^0 when the plastic boundary, assumed $Z_i+(\alpha-1)R$, reaches the effected target rear surface covering the projected area of πR^2 (see Fig. 1)

$$(Z_H-Z_T^0)^2+R^2=\alpha^2R^2. \tag{9}$$

After transition has been realized a spherical expansion flow field is assumed to be operative in the frontal zone II (see Fig. 2). To be consistent with Ref. [1] the flow field is given by Eq. (10). For later use, we define the variable r_1 by Eq. (11)

$$u_r=u\left(\frac{R}{r}\right)^2\cos\theta, \tag{10}$$

$$r_1\equiv\frac{R}{\sin\beta}. \tag{11}$$

Incompressible flow is assumed towards the free target rear surface in zone II (while zone I is considered a transition "dead zone" moving at velocity u), shown in Fig. 2. We consider the volume that is pushed by the penetrator from Z_T further to be equal to the volume of the spherical bulged zone, namely

$$\pi\eta_b^3R^3\frac{(1-\cos\beta)^2(2+\cos\beta)}{3\sin^3\beta}=\pi R^2(Z_T-Z_T^0), \tag{12}$$

$$Z_T=Z_T^0+\int_{t_T}^{t}u\,\mathrm{d}t, \tag{13}$$

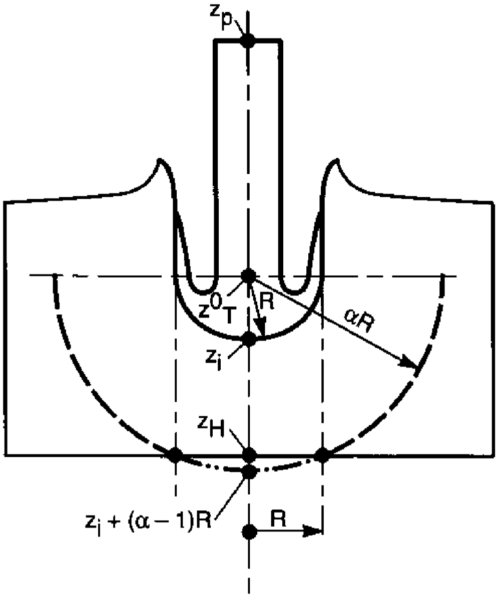
zp
z0T
R
αR
zi
zH
zi + (α − 1)R
R

Fig. 1. Transition to bulge formation.

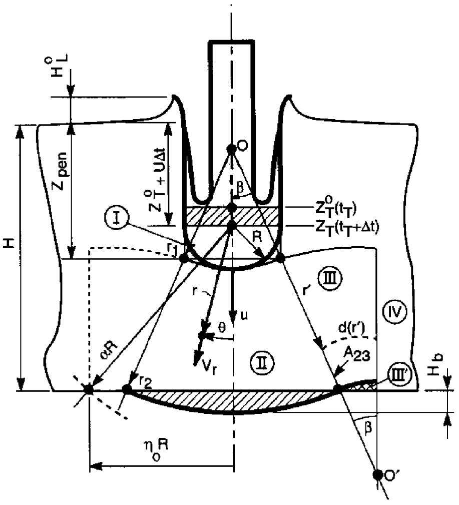
H0L
Zpen
Z0T + UΔt
H
O
β
Z0T(tT)
ZT(tT+Δt)
I
R
r1
III
r
r'
IV
u
θ
d(r')
A23
αR
Vr
II
r2
III'
Hb
β
ηoR
O'

Fig. 2. Bulge formation.

where Z_T^0 and t_T are the transition axial location and time, respectively, during the penetration process. The bulge radial extent $\eta_b R$ (Fig. 2) is given by Eq. (14), where $Z_{pen} = Z_H - Z_i + r_1 (1 - \cos\beta)$; and by utilizing Eq. (11), we get Eq. (15). Using Eqs. (14) and (15), and solving Eq. (12), we get $\beta(Z_T)$ and Eq. (16)

$$\eta_b = \frac{H - Z_{pen}}{R} \tan\beta + 1, \tag{14}$$

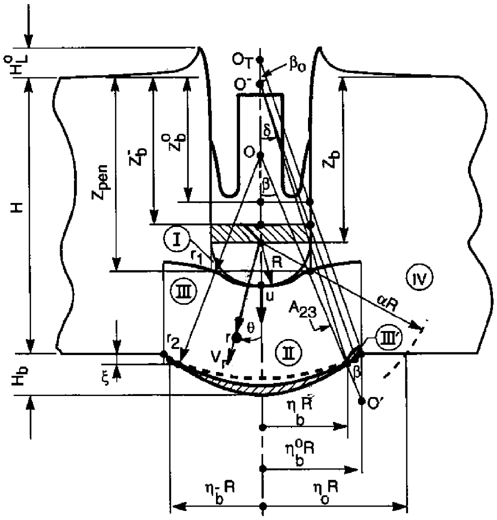

Fig. 3. Bulge advancement.

$$Z_{\text{pen}} = Z_{\text{H}} - Z_{\text{i}} + R\frac{1-\cos\beta}{\sin\beta}, \tag{15}$$

$$H_{\text{b}} = \frac{\eta_{\text{b}}R}{\sin\beta}(1-\cos\beta). \tag{16}$$

while $\eta_{\text{b}}R$ grows during bulge formation, assuming R is constant, η_{b} will finally come to a maximum value η_{b}^0 with associated $\beta_0 = \beta(\eta_{\text{b}}^0)$. $R\eta_{\text{b}}^0$ represents the maximum radial extent of the bulge. From this point z_{b}^0, the spherical growth of the bulge ceases. The bulge now advances in such a form that a new spherical sector is built over the former one (see Fig. 3) with the constraint that the volume is equal to that pushed by the penetrator from its former position.

Therefore, we can write

$$\frac{(1-\cos\beta)^2(2+\cos\beta)}{\sin^3\beta} - \frac{(1-\cos\delta)^2(2+\cos\delta)}{\sin^3\delta} - \frac{3u\Delta t}{\eta_{\text{b}}^3 R} = 0. \tag{17}$$

The following geometrical relationships are defined:

$$\delta = \sin^{-1}\left[\frac{\eta_{\text{b}}}{\eta_{\text{b}}^-}\sin\beta^-\right], \tag{18a}$$

$$\beta = \tan^{-1}\left[\frac{R(\eta_{\text{b}}-1)}{H+\xi-Z_{\text{pen}}}\right], \tag{18b}$$

$$\xi = \xi^- + \frac{\eta_{\text{b}}^- R}{\sin\beta^-}(\cos\delta - \cos\delta^-) \tag{19}$$

with Z_{pen} defined from Eq. (15). Eqs. (17)–(19) are solved simultaneously for the four unknowns β, $\delta, \eta_{\mathrm{b}}$, and ξ. The bulge height is given by

$$H_{\mathrm{b}} = \xi + \frac{\eta_{\mathrm{b}} R}{\sin\beta}(1 - \cos\beta). \tag{20}$$

Note: ξ^-, δ^-, β^- are previously calculated values, which were initially $0, \delta(\beta^0), \beta^0$ at Z_{b}^0.

2.2.2. Analyzing possible exit modes

Seven different exit modes have been assumed: ductile exit (Fig. 4), early brittle shear failure (BSF) (2 modes), BSF (3 modes) and fragmentation. Since the presentation of all these failure modes is long and the math involved is quite tedious it will be skipped in the core of the paper and left for the appendix. The failure condition for each of the failures modes is evaluated at each time step during the bulging deformation phase. The model "implements" the failure mode that occurs first.

2.3. Third phase: free flight

When the target "fails", that is, there is "perforation", the projectile no longer encounters any further resistance, but projectile erosion can continue some microseconds because of the large residual stresses in the plastic zone. Refs. [6,7] studies the history of the projectile length, as calculated using numerical simulations, for tungsten-alloy projectiles penetrating a 45.7-cm-thick RHA target. Behind the RHA target, separated by an air gap of 7.62 cm, is a RHA witness pack. Between exit from the rear surface of the target and the beginning of penetration into the witness pack, the projectile length decreases (erodes) by approximately one projectile diameter. This effect is not particularly large (nominally one part in 30 for this particular example) for single-plate

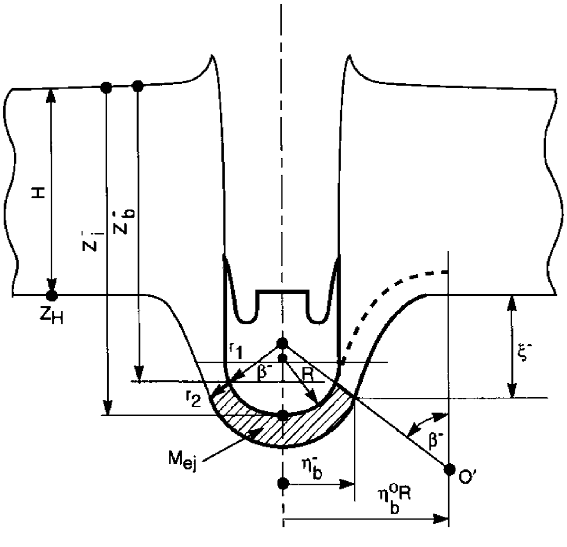

Fig. 4. Ductile exit.

targets, but the cumulative effect for multiple-plate targets would result in substantial errors and thus cannot be ignored.

2.4. Relaxation time

We are interested in cases where penetration stresses are sufficiently high that the projectile material is plastically deforming and eroding. The plastic extent in the projectile can be calculated with Eq. (5).

Using results from numerical simulations, it is possible to estimate the length of time it takes for the projectile to equilibrate in velocity. Elastic waves traveling within the projectile are responsible for velocity equilibration, so one possibility to estimate this relaxation time is to assume that it is proportional to the time it takes for an elastic wave to go and come back from nose to tail. But the results shown in Fig. 5 suggest that the relaxation time does not depend on projectile length. The plot shows the velocity of nose and tail of a long-rod tungsten-alloy projectile impacting a spaced target (six plates, vertical lines are the front of the plate). As the nose perforates a plate, the nose velocity increases, trying to equilibrate with the tail velocity. (Most of the projectile material has the speed of the tail [8], and therefore, the tail velocity—until the projectile becomes relatively short—dominates in determination of the equilibration velocity [9].) The time taken to relax between two consecutive plates does not depend on which plate is being penetrated. Consequently, since the projectile is shorter after each of the impacts, the relaxation time does not appear to depend strongly on the length of the projectile. More likely, the relaxation time depends on the size of the plastic zone in the projectile, which is proportional to the projectile radius.

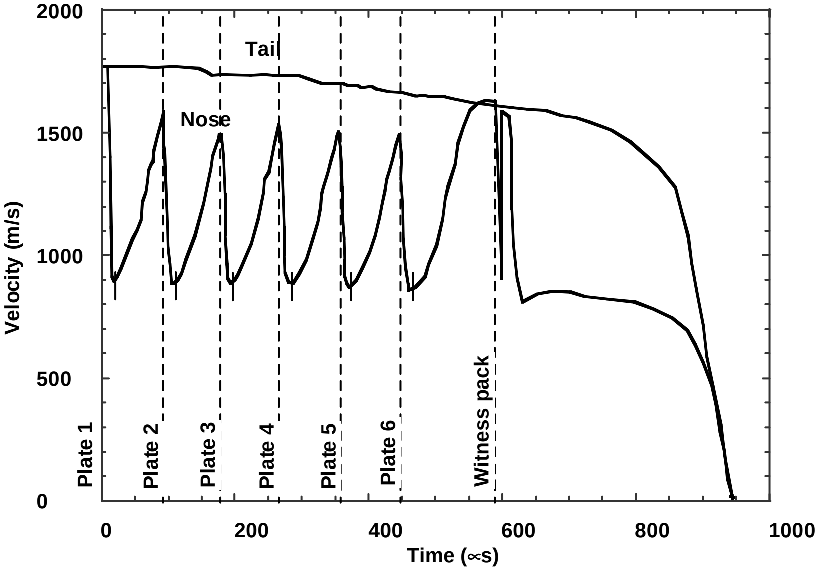

Fig. 5. Simulation results for nose and tail velocities of a tungsten-alloy projectile impacting six-spaced plates.

In this paper the time assumed for relaxation is given by

$$t_{\text{relax}} = 30\frac{R_{\text{p}}}{c_{\text{p}}}, \tag{21}$$

where R_{p} is the radius of the projectile and c_{p} the sound speed of the projectile material.

2.5. Velocity of the projectile after relaxation

Between failure of a plate and relaxation of projectile no force is acting on the projectile. The total momentum is then constant allowing the calculation of the velocity after relaxation. When the plate fails the velocity profile in the projectile is constant (say V_{fail}) from the tail to the rear of the plastic zone, and then decreases linearly in the plastic zone to the penetration velocity u_{fail}, see Refs. [1] for more details. Assuming that the length of the projectile just before failure is L_{fail}; the plastic extent s_{fail}; and the tail and nose velocities are V_{fail} and u_{fail}, respectively, then the velocity V_{relax} of the (now rigid) projectile after equilibration (relaxation) is given by

$$V_{\text{relax}} = \frac{(L_{\text{fail}} - s_{\text{fail}})}{L_{\text{fail}}}V_{\text{fail}} + \frac{s_{\text{fail}}}{L_{\text{fail}}}\left(\frac{V_{\text{fail}} + u_{\text{fail}}}{2}\right). \tag{22}$$

The projectile might impact the next target element before achieving total equilibration, as for example is shown in Fig. 5. Therefore Eq. (22) does not provide sufficient information, and an expression for the "nose velocity" u is needed for free flight.

2.6. Velocity of the nose and tail during free flight

The velocity of the nose during free flight is assumed to increase linearly with time from its velocity at the instant of failure, u_{fail}, to its equilibration velocity, V_{relax}

$$u(t) = u_{\text{fail}} + \left(\frac{V_{\text{relax}} - u_{\text{fail}}}{t_{\text{relax}} - t_{\text{fail}}}\right)(t - t_{\text{fail}}). \tag{23}$$

The same assumption gives the velocity of the tail

$$v(t) = v_{\text{fail}} + \left(\frac{V_{\text{relax}} - v_{\text{fail}}}{t_{\text{relax}} - t_{\text{fail}}}\right)(t - t_{\text{fail}}). \tag{24}$$

Eqs. (23) and (24) are valid only when $t < t_{\text{relax}}$. The position of the nose at any time as well as at the instant of the impact with the next target element are easily calculated with the integration of Eq. (23). The difference between Eqs. (23) and (24) gives the erosion rate (a negative quantity since the projectile is shortening); and integration of the erosion rate over time provides the decrease in projectile length.

Eqs. (1)–(24) and Eqs. (A.1)–(A.17), allow the solution of long-rod projectiles impacting semi-infinite or finite-spaced targets. The residual velocity and residual length from perforation of one target element are used as the "initial" conditions for impact with the next target element.

2.7. Examples

2.7.1. Calibration and examples with thick targets

An essential parameter in the perforation model is the uniaxial strain to failure ε_{cr}. One experiment was selected to calibrate the value of ε_{cr}. After calibration, the same ε_{cr} was used for the remainder of the model calculations. The experiment used for calibration was selected from experimental results reported in [10]. In the experiments, a 2.90-cm-thick hard-steel target will stop a $L/D = 12.5$ tungsten-alloy long-rod projectile ($L = 5.0\,\text{cm}$) impacting at 1240 m/s, but that same target is perforated at an impact velocity of 1260 m/s. This 1260-m/s result was selected as the limit case, permitting the solution of the equations at an "assumed" ballistic limit condition. The value for ε at arrest was then defined to be ε_{cr} (an error of approximately 20 m/s is thus introduced into the model, consistent with the uncertainty in the experimentally determined ballistic limit velocity). The analytical model requires as input the flow stresses for the projectile and target materials. The effective flow stresses were assumed to be 1.20 and 1.45 GPa, respectively, these values are commensurate with the material property values reported in [10]. ε_{cr} was determined to be 65% for the high-hard armor steel used in the experiments. As already mentioned, this value was then considered to be an intrinsic material property and was thus not varied as the model was exercised and the results compared to other experimental data.

The first example is the calculation of the penetration depth and bulge size for a plate with thickness (T) of 2.90 cm impacted by a tungsten long rod at 1240 m/s. The comparison of the experimental results and the analytical model is made in Fig. 6(a) for the ballistic limit condition. Model results are overlaid onto a photographic image of the test results. The black lines indicate the positions calculated by the analytical model. The total depth of penetration, the bulge height, and the lateral dimension of the bulge are reproduced very well by the analytical model. As can be seen, arrest of the projectile was also predicted.

The second case involves a 4.85-cm-thick target impacted by the same type of projectile, but now at 1680 m/s. The model predicts failure of the target (fragmentation failure mode), the failure

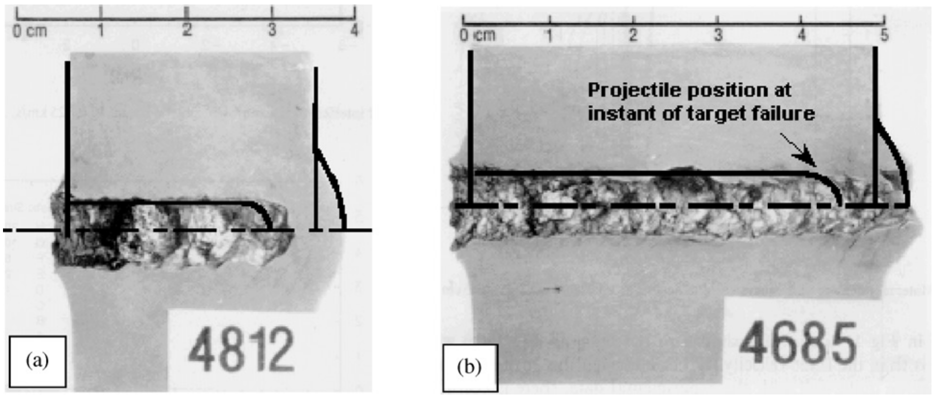

Fig. 6. Comparison of the analytical (black line) and experimental results. (a) $V_0 = 1240\,\text{m/s}$, $T = 2.90\,\text{cm}$, (b) $V_0 = 1680\,\text{m/s}$, $T = 4.85\,\text{m/s}$.

mode observed in the real test. Model results are again overlaid onto a photographic image of the test results, Fig. 6(b). Again the model correctly predicts the size and extent of the bulge.

The nose and tail positions as a function of time, using flash radiography, were also obtained for a number of experiments, all at an approximate impact velocity of 1700 m/s. These experimental points are shown in Fig. 7. The model results are shown as the solid lines. Thus, it is demonstrated that not only are the size of the bulge and failure well predicted, but that the time-histories of the projectile nose and tail agree extremely well with those measured in the experiments.

Another example is the analytical calculation of residual velocities and the ballistic limit velocity. It is well known that it is extremely difficult to obtain accurate results with a model near the ballistic limit because the derivative becomes infinite and the errors in the calculations increase accordingly. The example studied was a long rod, length 8.29 cm, impacting a steel target (Brinell Hardness 415), with a thickness of 2.90 cm. The experimental ballistic limit was determined to be 982 ± 35 m/s [10]. The yield strength values for tungsten (1.20 GPa) and steel (1.45 GPa) used in the analytical models are the ones used previously; ε_{cr} was again 65%. The results of the model are shown in Fig. 8, and compared to the experimental data. The ballistic limit predicted by the model was 1000 ± 25 m/s, which overlaps the experimental ballistic limit velocity. The model reproduces well the steep rise in residual velocity just above the ballistic limit velocity. The predicted residual velocities are only slightly higher than the experimental ones. This may be because all dissipative mechanisms have not been modeled. Alternatively, the steel might have been slightly different than the one used in the examples above (it almost certainly came from a different fabrication lot). Additionally, the projectile and target constitutive behaviors are simplified to single effective values for the flow stresses. Any or all of these effects could lead to slight discrepancies between model predictions and the experimental data. Given the approximations used in the analytical model to simplify and make tractable the mechanics, it is concluded that the model is quite accurate.

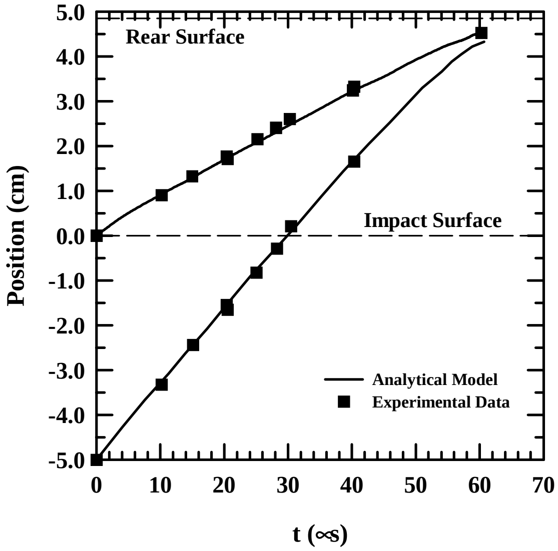

Fig. 7. Comparison between experiments and model of the nose and tail positions.

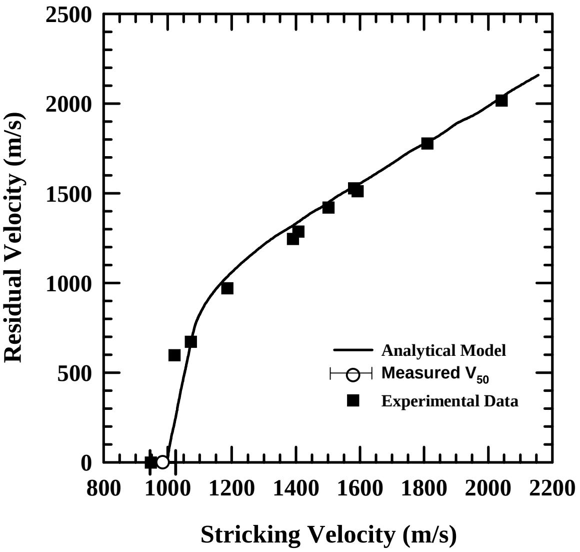

Fig. 8. Residual velocities obtained by the model compared with experiments.

Table 1
Projectile geometry

	Projectile 1	Projectile 2
Impact velocity (km/s)	1.775	2.60
Mass (g)	1830	850
Length (cm)	49.4	38.4
Diameter (cm)	1.65	1.28

2.7.2. *Examples with thick and thin and spaced targets*

Two multiple element target examples are presented, with each example having long-rod projectiles impacting at two different velocities. All the examples presented in this paper are taken from Ref. [6]; additional details on the experimental results are provided in Ref. [7]. The projectiles had a length-to-diameter (L/D) ratio of 30, and were equal kinetic energy projectiles. Information on the projectiles is summarized in Table 1. The targets are described later.

2.7.3. *Example of long rod against RHA target and witness pack*

This example is the impact of a tungsten-alloy, long-rod projectile penetrating a 45.72-cm-thick RHA target. Behind the target, separated by a 7.62-cm air gap, is a RHA witness pack. Tables 1 and 2 list the geometry and material properties used for the calculations. Fig. 9 shows both the numerical and analytical position vs. time plots for the two projectiles. The numerical simulation results, from the Eulerian wave code CTH, are shown as circles for clarity, although the output of the CTH are continuous lines. The CTH results matched the experimental depths of penetration into the witness pack, so the analytical model is compared to the time history numerical results. The predictions of the model are in excellent agreement with the numerical simulations.

Table 2
Material properties used in the analytical calculations

Projectile density (g/cm^3)	17.4	Target yield strength (GPa)	1.2
Projectile yield strength (GPa)	1.5	Target shear modulus (GPa)	77.7
Speed of sound in the projectile (km/s)	3.85	Target sound velocity (km/s)	4.50
Slope of Hugoniot (tungsten, n.d.)	1.44	Slope of Hugoniot (steel, n.d.)	1.49
Target density (g/cm^3)	7.85	Strain to failure in target (n.d.)	0.65

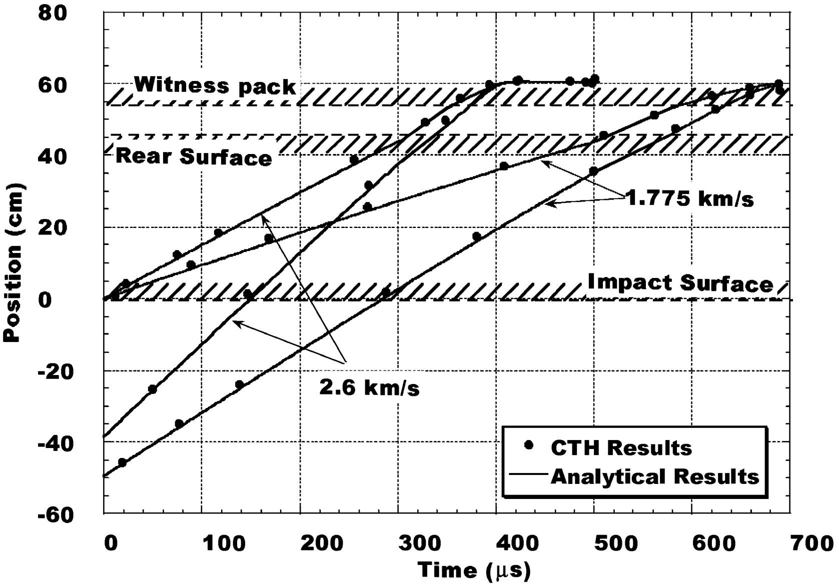

Fig. 9. Positions of tail and nose of the projectile calculated numerically (CTH) and analytically.

Fig. 10 depicts the history of velocities of the tail and nose for the two projectiles considered. It is pointed out that the peaks of the nose velocity happen when the projectile is in free flight. In this example, the air gap of 7.62 cm is sufficiently wide to allow for the projectile velocity to equilibrate (relax) completely before impacting the witness plate. The agreement between the model and the numerical simulations is again very good during penetration of the RHA target and during the free flight. The agreement is not quite so good in the penetration of the witness pack because the projectile, by this time, has a low aspect ratio, and the assumption that the tail portion of the projectile is in a state of uniaxial stress is no longer valid. Nevertheless, overall agreement is quite good.

2.7.4. *Example of long rod against six-spaced plates and witness pack*

In this example, the long rods (same as in the first example) were fired against six high-hard steel plates, each 1.90-cm thick, inclined at 65° (NATO angle), and separated by air gaps of 2.54 cm. The witness pack was placed 7.62 cm behind the last plate. To account for target obliquity in the

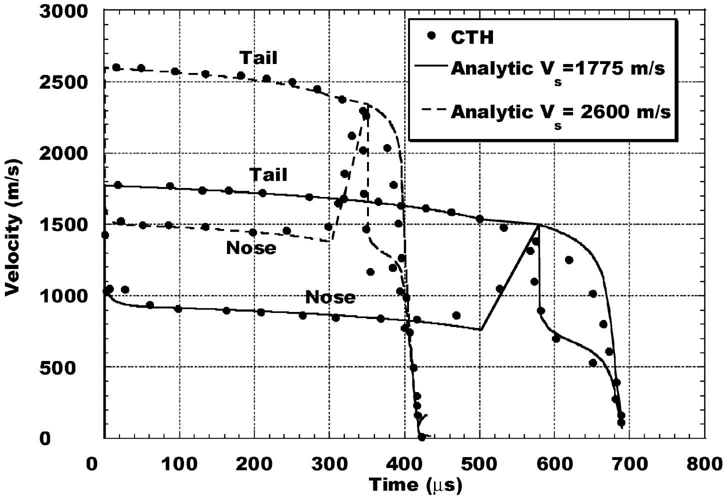

Fig. 10. Time histories of the tail and nose velocities for numerical (CTH) and analytical model results.

analytical model, it was assumed that the effective plate thicknesses should be the line-of-sight thicknesses as seen by the projectile. Therefore, the target elements were increased by 1/cos 65°.

It is more difficult to assess the accuracy for this example. The numerical simulations overpredicted the depth of penetration into the witness pack, at each of the impact velocities, by approximately 4 cm. Most likely, this is due to an inadequate treatment of failure at the projectile nose and/or breakout (failure) from each of the target elements. Unfortunately, however, the depth of penetration into the witness pack is essentially the only diagnostic from the experiment. Numerical simulations provide time histories of penetration, which allow for better comparisons, so comparisons are made with the simulation results.

Position vs. time for the fast and slow projectiles from the simulations and the analytical model are compared in Fig. 11; again, the circles represent the simulations results, and the lines the results from the analytical model. Agreement is very good for the 2.60-km/s projectile. For the lower velocity projectile the analytical model underpredicts the depth of penetration into the witness pack, but is in better agreement with the experimental results.

The time histories of the nose and tail of the projectiles are plotted in Fig. 12. Predictions of the analytical model are in very good agreement for the hypervelocity projectile. For the 1.775-km/s projectile, a shift between the analytical and numerical calculations is observed in the impact timing. The cause for this shift is that the numerical calculation is three-dimensional, allowing for the formation of an asymmetric mushroom head on the nose of the projectile. (An asymmetric mushroom nose also forms on the 2.60-km/s projectile, but the diameter of this projectile is smaller, and therefore, the effect is less pronounced. Further, the velocity is higher, so strength effects are not as significant as at the lower velocity.) Because of the obliquity of the target plates, the "side" of the mushroom impacts the plates and interaction starts sooner than for normal impact. Multiple applications of this affect results in a cumulative shift in the time. The analytical model does not predict as deep penetration as the numerical simulations, as already discussed, so the total time of penetration is correspondingly less.

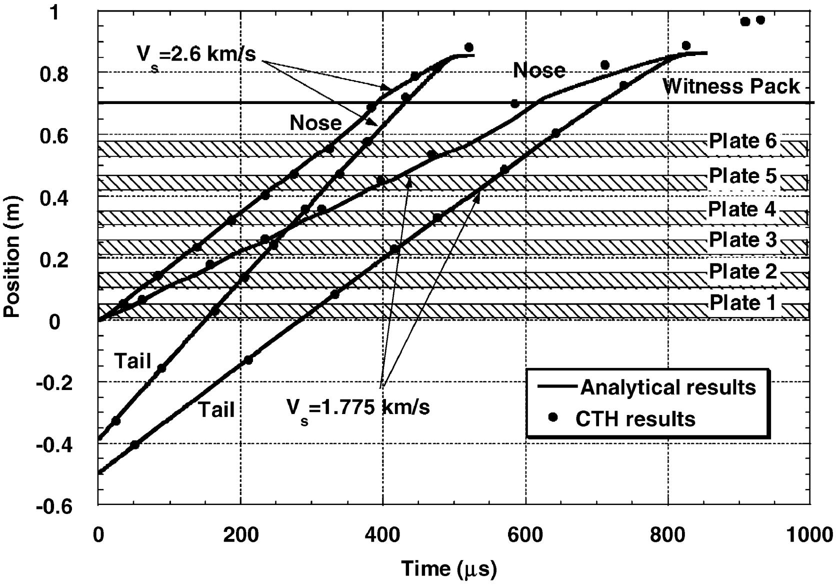

Fig. 11. Position–time histories for numerical (CTH) and analytical models for the six-plate impact example.

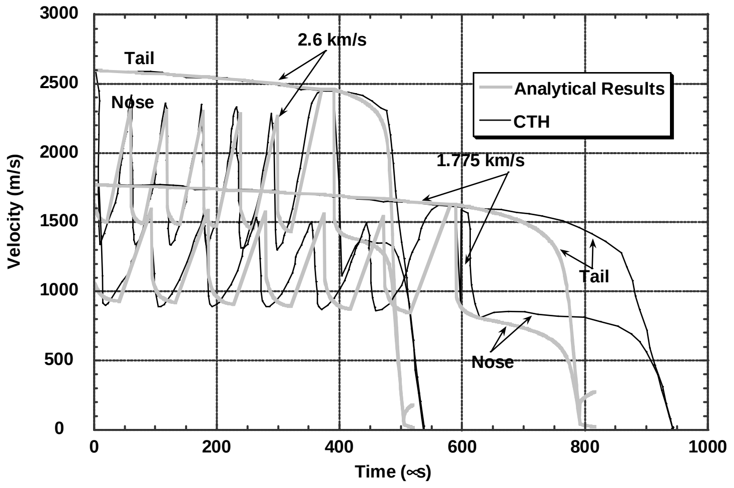

Fig. 12. Time histories of the tail and nose velocities for numerical (CTH) and analytical model for the six-plate impact example.

3. Conclusions

A blending of two well-known penetration models, Walker–Anderson and Ravid–Bodner, has been performed. The penetration mechanics of long rods into multiple metallic plates has been divided into three main phases: semi-infinite penetration phase (before the plastic front reaches the back of the target); bulging and failure phase; and the last phase, a relaxation phase, which occurs during "free flight" of the projectile prior to impacting another target element. The Walker–Anderson model was used to describe the semi-infinite penetration process while the Ravid–Bodner exit stages were implemented for the second stage. The free-flight stage model was developed based on simple assumptions drawn from the results of numerical simulations and momentum conservation. The three models were combined to form a "unified" model. The unified model is able to predict a wide range of penetration mechanics phenomena including semi-infinite penetration, penetration into finite-thick and thin plates, and penetration into spaced plates. The model has been validated against computations and experiments, matching histories of velocities of nose and tail and ballistic limits quite remarkably. The primary discrepancy is found to occur at the end of the penetration process where the assumption of uniaxial stress within the projectile is no longer correct. The authors are currently working to improve this aspect of the model.

Appendix. Seven failure modes

For the exit modes, the flow on the interface between zones II and III is assumed to be

$$u_r = u\left(\frac{R}{r}\right)^2 \frac{\cos\beta}{\sin^2\beta},$$

where r is now defined from point 0 (see Figs. 2 and 3).

Ductile exit

If no other failure criteria are met or if no failure occurs during penetration into a ductile target plate, then the process described above will continue while β becomes larger and larger, and $\eta_b \to 1.0$. In this case a spherical cape (M_{ej}) will be ejected in front of the residual penetrator with the onset of a mechanical instability, defined by

$$Z_b^- + u\,\Delta t - R(1-\cos\beta^-) \geqslant \xi^- + H. \tag{A.1}$$

Early brittle shear exit modes

There are two early failure modes, designated *EBS1* and *EBS2*. Early failure is considered if it occurs during bulge formation (Fig. 2).

EBS1: In zone III of Fig. 2, we can calculate the shear strain rate

$$\dot{\gamma}_3 = \frac{R^2 u \cot\beta}{\beta (r')^2 (\eta_0 R - r' \sin\beta)}, \tag{A.2a}$$

while β is in radians and r' is defined and shown in Fig. 2. It is assumed that the interface A_{23} does not fail and that it moves with the prescribed flow velocity of zone II where $\theta \equiv \beta$. Material deformation at the zone IV interface can be neglected in comparison to zone III, which is subjected to extensive shear. $\dot{\gamma}_3$ can be now integrated over the volume of zone III (V_{III}) to get

$(\dot{\gamma}_3)_{\mathrm{avg}}$, where $(\dot{\gamma}_3)_{\mathrm{avg}}$ is defined as

$$(\dot{\gamma}_3)_{\mathrm{avg}} = \frac{\int \dot{\gamma}_3 \, \mathrm{d}V_{\mathrm{III}}}{V_{\mathrm{III}}}. \tag{A.2b}$$

Using Eqs. (A.2a) and (A.2b) we get that

$$(\dot{\gamma}_3)_{\mathrm{avg}} = \frac{u \sin(2\beta) A_1}{\beta R(\eta_0 A_3 - A_2)}, \tag{A.3a}$$

$$A_1 = \frac{\eta_0}{\eta_{\mathrm{b}}}(\eta_{\mathrm{b}} - 1)\left(1 - \frac{1}{2\cos(\beta/2)}\right) + \frac{\ln(\eta_{\mathrm{b}})}{2\cos(\beta/2)}, \tag{A.3b}$$

$$A_2 = \frac{2}{3} \frac{(\eta_0 - 1)^3 - (\eta_0 - \eta_{\mathrm{b}})^3}{\beta \cot(\beta/2)}, \tag{A.3c}$$

$$A_3 = (\eta_0 - 1)^2 - (\eta_0 - \eta_{\mathrm{b}})^2. \tag{A.3d}$$

Failure occurs when

$$\int_{t_{\mathrm{T}}}^{t} (\dot{\gamma}_3)_{\mathrm{avg}} \, \mathrm{d}t \geqslant \gamma_{\mathrm{cr}}, \tag{A.4}$$

where t_{T} is the time of the beginning of the bulge phase, γ_{cr} is a material property; $\gamma_{\mathrm{cr}} \approx \sqrt{3}\varepsilon_{\mathrm{cr}}$ where $\varepsilon_{\mathrm{cr}}$ is usually calculated from an uniaxial tension test by measuring the elongation strain at failure and reduction of area at failure.

EBS2: It might occur that the accumulated strain rate on the area of A_{23} (between zones II and III, see Fig. 2) will result in a shear strain that exceeds γ_{cr}. Therefore, we can calculate $(\dot{\gamma}_{23})_{\mathrm{avg}}$

$$(\dot{\gamma}_{23})_{\mathrm{avg}} = \frac{\int \dot{\gamma}_3 \, \mathrm{d}A_{23}}{A_{23}} \tag{A.5a}$$

and obtain

$$(\dot{\gamma}_{23})_{\mathrm{avg}} = \frac{u \sin(2\beta)}{\beta R} A_4, \tag{A.5b}$$

$$A_4 = \frac{\ln\left(\eta_{\mathrm{b}} \dfrac{\eta_0 - 1}{\eta_0 - \eta_{\mathrm{b}}}\right)}{\eta_0(\eta_{\mathrm{b}}^2 - 1)}. \tag{A.5c}$$

The failure criterion at time $t = t_{\mathrm{f}}$ for *EBS2* is

$$\int_{t_{\mathrm{T}}}^{t} (\dot{\gamma}_{23})_{\mathrm{avg}} \, \mathrm{d}t \geqslant \gamma_{\mathrm{cr}}. \tag{A.6}$$

Brittle shear failure (BSF)

There are three different BSF modes that can occur during the bulge advancement stage (Fig. 3), these are designated *BSF1*, *BSF2*, and *BSF3*, respectively.

BSF1: This corresponds to failure of zone III of Fig. 3 due to the accumulated shear strain. The calculation is similar to *EBS1* except the radial extension of zone III is now defined as $R\eta_b^0$ instead of $R\eta_0$ as in the case of *EBS1*. Therefore, the calculation is similar to *EBS1* except that η_b^0 replaces η_0 in Eqs. (A.2a) and (A.3a)–(A.3d). Then Eq. (A.4) applies for *BSF1*.

BSF2: This corresponds to failure of the interface area between zones II and III of Fig. 3. The calculation is again the same as for *EBS2* where η_b^0 replaces η_0 in Eq. (A.5c), which modifies Eq. (A.5b). Then, Eq. (A.6) holds for *BSF2*.

BSF3: If it is also possible to get fracture at layers of zone III on the peripheral spalling zone within zone III of Fig. 3, denoted as zone III′ in this case:

$$\gamma_{\text{out}} \equiv \frac{\xi}{R(\eta_b^0 - \eta_b)} \tag{A.7}$$

and if $\gamma_{\text{out}} \geqslant \gamma_{\text{cr}}$ failure *BSF3* occurs.

Fractured ejected mass

The possibility of fragmentation exit mode (FEM) is examined utilizing two basic assumptions: (a) failure occurs at zone II of Fig. 2 or Fig. 3 when $(\varepsilon_{\text{eff}})_{\text{avg}}$ of that zone is greater than ε_{cr}; (b) fragmentation of this zone is in accordance with the Grady criteria [11]. For the first assumption, we will use the definition of the flow field from Ref. [1], which the strain rates can be calculated

$$\dot{\varepsilon}_{rr} = -2u\left(\frac{R^2}{r^3}\right)\cos\theta, \tag{A.8}$$

$$\dot{\varepsilon}_{\theta\theta} = u\left(\frac{R^2}{r^3}\right)\cos\theta, \tag{A.9}$$

$$\dot{\varepsilon}_{r\theta} = -\frac{1}{2}u\left(\frac{R^2}{r^3}\right)\sin\theta. \tag{A.10}$$

We can define

$$\dot{\varepsilon}_{\text{eff}} = \sqrt{\tfrac{2}{3}\dot{\varepsilon}_{ij}\dot{\varepsilon}_{ij}} \tag{A.11}$$

and for zone II we get

$$(\dot{\varepsilon}_{\text{eff}})_{\text{avg}} = \frac{\int \dot{\varepsilon}_{\text{eff}}\,\mathrm{d}V_{\text{II}}}{V_{\text{II}}},$$

thus getting

$$(\dot{\varepsilon}_{\text{eff}})_{\text{avg}} = \frac{3u\sin^5(\beta)\ln(\eta_b)g(\beta)}{R(\eta_b^3 - 1)(1-\cos\beta)}, \tag{A.12}$$

where

$$g(\beta) = \frac{1}{\sin^2 \beta}\left\{(1 - \cos\beta)A_6 + \frac{1}{\sqrt{132}}\ln\frac{1+\sqrt{\frac{11}{12}}}{\sqrt{\frac{11}{12}}\cos\beta + A_6}\right\}, \tag{A.13a}$$

$$A_6 = \sqrt{1 - \tfrac{11}{12}\sin^2\beta}. \tag{A.13b}$$

Failure occurs at $t = t_f$ when

$$\int_{t_T}^{t_f} (\dot{\varepsilon}_{\mathrm{eff}})_{\mathrm{avg}}\, \mathrm{d}t > \varepsilon_{\mathrm{cr}}. \tag{A.14}$$

Fragmentation of this failure zone II of Fig. 2 or Fig. 3 (depending on time of occurrence) is in accordance with Grady (Kipp and Grady, 1996); therefore, the brittle fractured fragment (see Fig. 13) will have a radial dimension (thickness) given by Eq. (A.15), where $\dot{\varepsilon}_{\mathrm{eff}}$ is defined in Eq. (A.11) as a function of r. After substitution of Eqs. (A.8)–(A.10) into Eq. (A.11), and solving for zone II, we obtain Eq. (A.12) and its area $A_f(r)$, which is defined by Eq. (A.16)

$$\Delta r(r) = \left[\frac{\sqrt{24}K_{\mathrm{Ic}}}{\rho c_0 \dot{\varepsilon}_{\mathrm{eff}}}\right]^{2/3}, \tag{A.15}$$

$$A_f(r) = \pi\left[\frac{\sqrt{24}K_{\mathrm{Ic}}}{\rho c_0 \dot{\varepsilon}_{\mathrm{eff}}}\right]^{4/3}. \tag{A.16}$$

Thus, the spherical sectored fragment can be defined symmetrically $r\Delta\theta \approx r\Delta\phi \equiv \Delta$, see Fig. 13, and therefore, we get Eq. (A.17). Utilizing Eqs. (A.15) and (A.16), we solve Eq. (A.17) for Δ.

$$A_f(r) \approx 2\Delta^2 + 4\Delta r(r)\Delta. \tag{A.17}$$

Zone II will be fragmented at a distance r while assuming $\Delta\phi = \Delta\theta = \Delta r$. The fragments will be ejected at their current velocity.

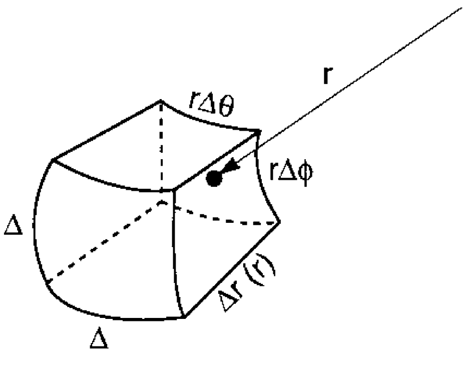

Fig. 13. Zone II fragment shape.

References

[1] Walker JD, Anderson Jr CE. A time-dependent model for long-rod penetration. Int J Impact Eng 1995;16(1): 19–48.

[2] Ravid M, Bodner SR. Dynamic perforation of viscoplastic plates by rigid projectiles. Int J Impact Eng 1983;21(6):577–91.

[3] Ravid M, Bodner SR, Holcman I. A two-dimensional analysis of penetration by an eroding projectile. Int J Impact Eng 1994;15(5):587–603.

[4] Ravid M, Bodner SR, Walker JD, Chocron S, Anderson Jr CE, Riegel III JR. Modification of the Walker–Anderson penetration model to include exit failure modes and fragmentation. Proceedings of the 17th International Symposium on Ballistics. vol. 3, Midrand, South Africa, March 23–27, 1998. p. 267–74.

[5] Chocron S, Anderson Jr CE, Walker JD. Long-rod penetration: cylindrical vs. spherical cavity expansion for extent of plastic flow. Proceedings of the 17th International Symposium on Ballistics, vol. 3, Midrand, South Africa, March 23–27, 1998. p. 319–26.

[6] Anderson Jr CE. Littlefield DL. Pretest predictions of long-rod interactions with armor technology targets, SwRI Report 07-5117, prepared for the US Army Research Office, Southwest Research Institute, San Antonio, TX, April, 1994.

[7] Anderson Jr CE, Bless SJ, Littlefield DL, Subramanian R. Prediction of large scale impact experiments on steel targets. Proceedings of the 14th International Symposium On Ballistics, vol. 2, Québec, Canada, September 26–29, 1993. p. 459–68.

[8] Anderson Jr CE, Walker JD. An examination of long-rod penetration. Int J Impact Eng 1991;11(4):481–501.

[9] Anderson Jr CE, Holer V, Walker JD, Stilp AJ. The influence of projectile hardness on ballistic performance. Int J Impact Eng 1999;22(6):619–32.

[10] Anderson Jr CE, Holer V, Walker JD, Stilp AJ. Time-resolved penetration of long rods into steel targets. Int J Impact Eng 1995;16(1):1–18.

[11] Grady DE, Kipp ME. Fragmentation of solids under dynamic loading, in structural failure. In: Werzbek T, Jones N, (Eds). NY, John Wiley & Sons, 1989, pp. 1–40.